

# Low dimensional modeling of a non-uniform, buckled piezoelectric beam for vibrational energy harvesting

Louis Van Blarigan<sup>1</sup>, Jeff Moehlis<sup>1</sup> and Robert McMeeking<sup>1,2,3</sup>

<sup>1</sup>Department of Mechanical Engineering, University of California, Santa Barbara, CA 93106, USA

<sup>2</sup>Materials Department, University of California, Santa Barbara, CA 93106, USA

<sup>3</sup>School of Engineering, Aberdeen University, King's College, Aberdeen AB24 3UE, Scotland

E-mail: [louis01@umail.ucsb.edu](mailto:louis01@umail.ucsb.edu)

Received 8 January 2015, revised 17 March 2015

Accepted for publication 7 April 2015

Published 7 May 2015



CrossMark

## Abstract

A model is developed for a non-uniform piezoelectric beam suitable for analyzing energy harvesting behavior. System dynamics are projected onto a numerically developed basis to produce energy functions which are used to derive equations of motion for the system. The resulting model reproduces the experimentally observed transition to chaos while providing a conservative estimate of power output and bandwidth.

Keywords: piezoelectric, energy harvesting, solid mechanics

(Some figures may appear in colour only in the online journal)

## 1. Introduction

Vibrational energy harvesting allows small amounts of power to be extracted from otherwise wasted ambient energy sources. Capturing this energy provides a power source for small electronic devices without the need for batteries or wires and power supplies, thus reducing installation/maintenance costs. Piezoelectric systems are an attractive approach to vibrational energy harvesting because of their high power density [1] and ease of construction. Many piezoelectric energy harvesters have been proposed and experimentally demonstrated, utilizing both linear and nonlinear approaches; a few examples can be seen in [2–7]. Linear devices typically utilize a beam in a cantilever configuration with a piezoelectric portion that converts mechanical deformation into electrical energy. This type of device is well understood and modeled, but the bandwidth over which energy can be harvested is very small. A detailed discussion of modeling these linear systems can be seen in [8]. However, naturally occurring vibrations tend to have a mixed frequency content which can be time varying, implying that widening the bandwidth over which appreciable energy can be harvested can lead to better performance. Several devices have been proposed to incorporate nonlinearity to enhance the bandwidth of energy recovery, commonly achieved through bi-

stability induced either through a buckled beam or magnetic instabilities [9]. Buckled beams are particularly attractive because construction of these devices is accomplished with minimal additional components. While the theory of modeling buckled beams has been developed [10], its application to piezoelectric energy harvesting has been lacking.

Piezoelectric materials couple between mechanical deformation and electrical field generation. The direct piezoelectric effect is when a stress field causes charge surpluses at its surface, usually detected through a potential difference across the specimen. Alternatively, the converse piezoelectric effect is when an electric field applied to the material causes a strain to develop. Due to this coupling, piezoelectric materials need to be modeled in the mechanical and electrical domain simultaneously. Previous modeling attempts have included Masana and Daqaq [11], who considered axially loaded piezoelectric structures below the critical buckling load. Sneller *et al* [12] generated a single-mode model using the theory developed by [10], but did not consider the converse piezoelectric effect. Cottone *et al* [13] generated a single-mode Galerkin projection for a piezoelectric buckled beam, but the mode shape was calculated about the unbuckled position, and the resulting model required extensive parameter tuning to enable the response to resemble the experimental data.

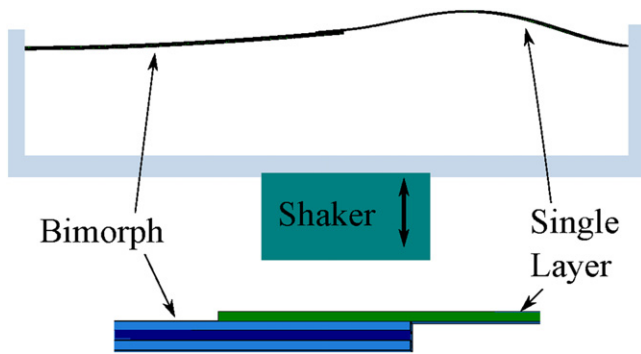


**Figure 1.** Cartoon of beam setup mimicking the experimental device. The fixed ends are approximately 20 cm apart and the overlap is approximately 10 mm. The lower detail is a zoomed in view of the joint and is not to scale with the rest of the image.

In this paper a model is generated for a non-uniform buckled beam, using  $d_{33}$  mode beams commercially available from Advanced Ceramics Inc. [14]. The experimental system and methods are detailed in [15], but the experiments performed in this paper operate at a different beam length and buckling level than the previously published work, which lowers the input power level at which appreciable energy can be harvested. A numerical analysis is used to develop a basis onto which the system dynamics are projected in order to derive a low-dimensional model. This technique allows an analytic model to be developed for a system that was previously intractable. The resulting model is designed to reproduce the dynamic behavior seen in the experiment, with the intention of providing a platform for in-depth dynamic analysis of the underlying phenomena. Due to the complex nature of the experiment, and the severe truncation required to construct a model appropriate for dynamic analysis, perfect agreement between model and experiment is neither expected nor achieved; however, the model is able to successfully capture the key features of the dynamics.

## 2. Experimental device

In a transversely isotropic piezoelectric material, coupling between mechanical deformation and electric field can be described with three non-zero constants:  $d_{31}$ ,  $d_{33}$ , and  $d_{15}$ . The first subscript refers to the direction in which the electric field is measured, and the second subscript denotes in Voigt notation the direction of mechanical deformation. In piezoelectric materials the poling direction is defined as the three-direction. In the most commonly used piezoelectric material, PZT,  $d_{15}$  is highest, followed by  $d_{33}$ , and the lowest is  $d_{31}$ . Most piezoelectric energy harvesters have utilized setups that capture electric fields created by the  $d_{31}$  coupling because electrode placement is very simple. While  $d_{31}$  piezoelectrics are simple to construct, a larger coupling coefficient, and therefore better efficiency, can be realized by designing to utilize the  $d_{33}$  orientation.

The experimental device consists of a nonuniform piezoelectric beam in a buckled configuration, as seen in figure 1.

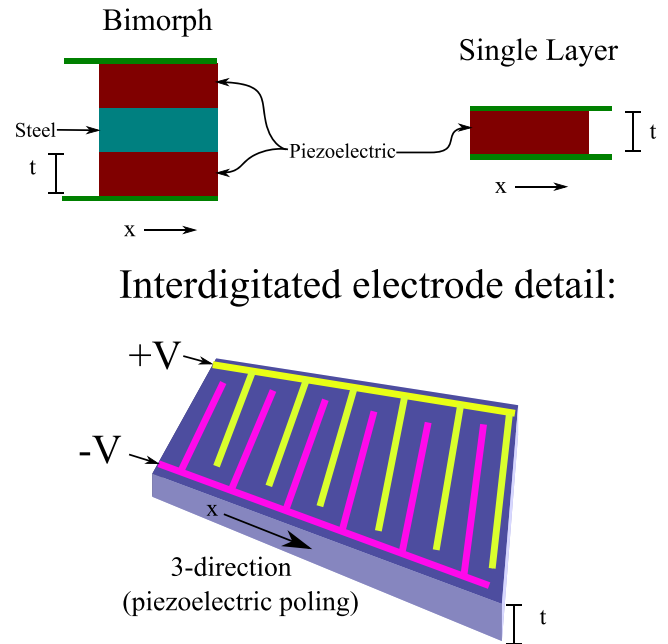


**Figure 2.** Upper panel shows basic construction of bimorph beam on the left, and a single layer of piezoelectric material on the right. The axial direction in the beam is identified by the coordinate  $x$ , while the thickness of the beam is indicated by  $t$ . Layers on top and bottom of bulk piezoelectric material represent layers of interdigitated electrodes, detailed in the lower panel. Not shown in this view is that there are two layers of interdigitated electrodes along the steel shim. Note that the interdigitated electrodes detect electric fields in the axial direction, denoted as  $x$  in the drawings, which coincides with the poling direction of the piezoelectric material and is therefore defined as the three-direction.

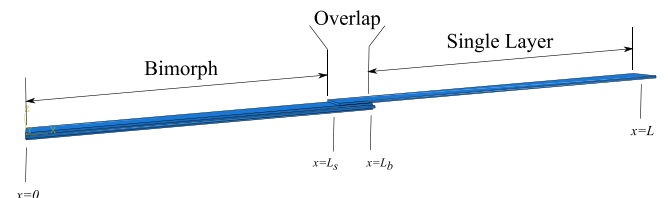


**Figure 3.** Model construction imitating experimental setup, showing different beam sections and how they are connected. The axial coordinate  $x$  runs from 0 at the left-hand end of the beam to  $L$  at the right-hand end. Both ends ( $x = 0, L$ ) are constrained with clamped boundary conditions.

The beam is constructed from two flexible ceramic piezoelectric elements from Advanced Ceramics, Inc. [14]: a single-layer element (catalog #PFC-W14) and a bimorph element (catalog #PFCB-W14). The piezoelectric layers in these beams are designed in a  $d_{33}$  configuration; the interdigitated electrodes detect electric fields in the axial direction, thus utilizing the  $d_{33}$  coupling coefficient. The bimorph is constructed by placing a steel core between two piezoelectric layers as shown in figure 2, so that bending the beam produces an axial deformation in the piezoelectric material. Bimorph and single-layer elements are bonded together as shown in figure 3 with  $\approx 10$  mm overlap, and the other ends are clamped to prevent displacement or rotation. The mount is attached to a voice coil shaker and shaken

vertically. This experimental device has been shown to generate a significant power output with a bandwidth larger than a cantilevered bimorph beam [15]. Moreover, the beam has been shown to produce significant power output when the resulting behavior is chaotic.

### 3. Model derivation

The method selected for modeling this system involves determining the buckled equilibrium position, finding natural modes about this equilibrium position, and projecting them onto an energy function. This will be used to derive equations of motion for the beam where the independent variables are the amplitudes of the natural modes and the equilibrium shape. Due to the complexity of the experimental system, analytic solutions as pursued in [10] are not available. To overcome this obstacle, finite element analysis (FEA) is used to determine both the equilibrium shape and the natural modes about that operating point.

Symmetry is assumed for both the buckled equilibrium and each beam's cross-section relative to the respective neutral axis. All motions of the beam are assumed to be transverse because the width of the beam is much greater than the thickness. The fixed end of the bimorph beam is defined to be at  $x = 0$ , and the fixed end of the single-layer beam is at  $x = L$ . Integrals over the length of the beam are to be broken into two separate ones each with uniform material parameters: one over the length of the bimorph, and one over the length of the single-layer beam:

$$\int_0^L (\cdot) dx \approx \int_0^{L_b} (\cdot) dx + \int_{L_s}^L (\cdot) dx, \quad (1)$$

where  $L_b$  is the point in the beam where the bimorph section ends, and  $L_s$  is the point in the beam where the single-layer beam begins (see figure 3). The beams overlap between  $L_s$  and  $L_b$ ; note that this region is included in both integrals above. Dealing with the overlapping region in this manner is an approximation that simplifies computations while maintaining the proper mass distribution. Electric fields in the material that are not detected by the electrodes are assumed to provide negligible contributions to the dynamics and are ignored. The response of the material at fixed electric field is assumed to be linear.

#### 3.1. Mode generation

The FEA software ABAQUS [17] has been used to construct a model of the beam. The model is constructed from two basic units: a steel shim and a piezoelectric beam. The dimensions and important material parameters (experimentally determined) of each section can be seen in table 1. These units are assembled into a structure equivalent to the experimental setup as seen in figure 3. Both free ends of the assembly are constrained as fixed boundary conditions, allowing no translation or rotation to occur at the clamping points. A cartoon representation of the setup can be seen in figure 1. To model the buckled equilibrium, the axial degree of freedom is

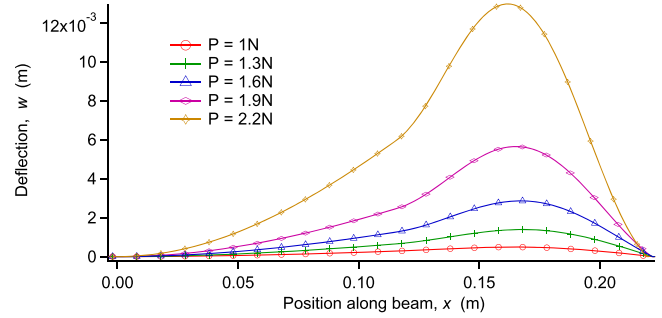


**Figure 4.** Evolution of buckled equilibrium position with axial loads between 1 and 2.2 N. Note that the right-hand side of the beam, which consists of the single-layer portion, exhibits much larger deviations from the centerline than the bimorph section. In this paper, the curve at  $P = 1.3$  N will be used for analysis.

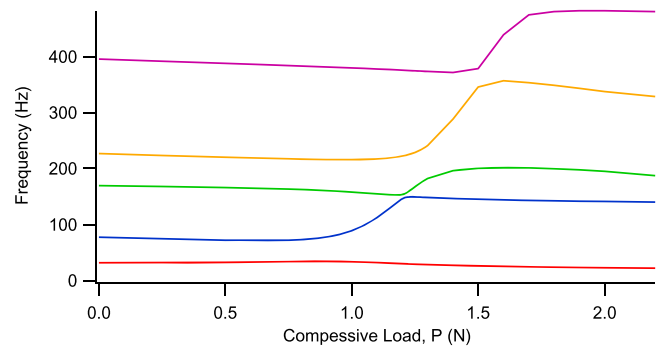


**Figure 5.** Dependence of natural frequencies on the axial compressive load. Note that eigenvalues two and three come very close together when the axial load is approximately 1.25 N. Analytic predictions for buckled beams indicate that there should be an eigenvalue crossing between the second and third eigenvalues. Examined closely it is clear that these eigenvalues do not cross in this example, but independently evolve through this region. The difference between observed model behavior and expected analytic behavior is due to the symmetry breaking of the bonded joint. The region where these eigenvalues approach each other has been found to be a promising energy harvesting region.

**Table 1.** Material parameters for the two different sections used to build the finite element model.

	Steel shim	Piezoelectric
Width (mm)	14	10
Height (mm)	0.4	0.4
Length (mm)	116	116
Mass/length ( $\text{g mm}^{-1}$ )	0.045	0.015
Modulus (GPa)	180	15.2
Poisson ratio	0.3	0.3

allowed to translate and an axial force is applied. A quasi-static analysis then determines the resulting buckled configuration, as seen in figure 4. Thereafter the axial degree of freedom is fixed, and a linear frequency analysis is performed to extract mode shapes (denoted  $[U]_{(i)}$ ) and the associated natural frequencies about the buckled equilibrium configuration. The mode shapes and their associated frequencies are not constant as the degree of buckling changes, similar to the

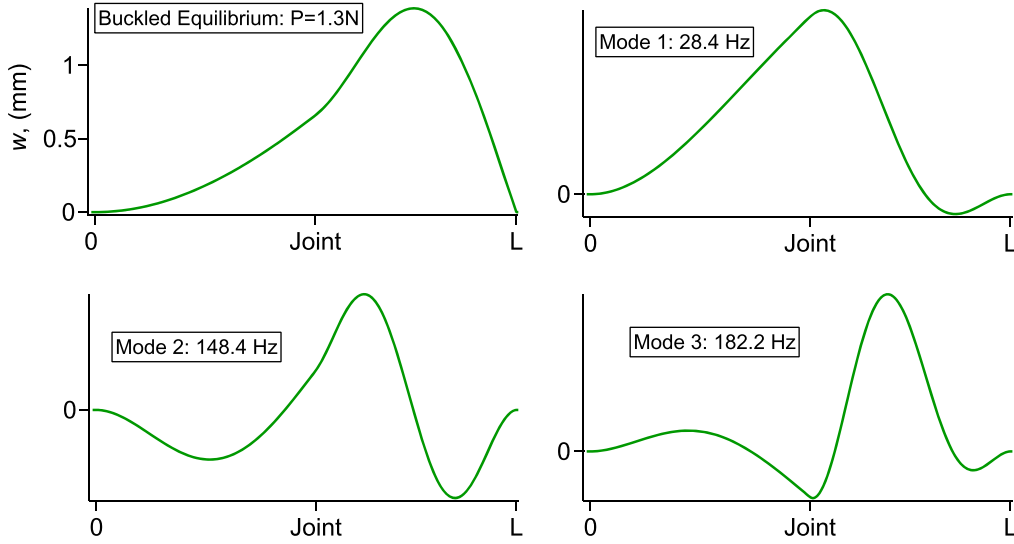


**Figure 6.** Buckled equilibrium state in terms of transverse displacement and the first three normal modes with their associated frequencies about the buckled equilibrium with axial load of 1.3 N. The horizontal axis represents the distance along the beam from 0 to  $L$ , while the vertical axis portrays the transverse deflection, actual for the buckled equilibrium mode and normalized for the linear modes.

analytic solutions in [10] for a simple buckled beam. The dependence of the associated frequencies on the compressive load can be seen in figure 5. The linear mode shapes are computed so that they are orthogonal with respect to the finite element mass matrix  $[M]$ :

$$[0] = [U]_{(i+1)}^T [M] [U]_{(i)}. \quad (2)$$

However, these modes are not orthogonal to the buckled equilibrium shape. Examining the components of the displacement, we find that the out-of-plane motions are several orders of magnitude lower than those in the transverse and axial directions and will be assumed to be negligible in the frequency range of interest. The axial motion ( $u$ ) is critical to determining the buckled configuration, but subsequently any axial motion due to oscillations about the buckled equilibrium are very small compared to the transverse motions. Therefore we will consider the axial motion fixed after the initial buckling, and assume that only transverse motions ( $w$ ) of the beam are significant to time varying energy storage. Assuming that the time and spatial dependence of  $w$  can be separated and any arbitrary beam shape can be reconstructed by linear combinations of the mode shapes, we write the displacement functions as

$$u(x) = u_c(x), \quad (3)$$

$$w(x, t) = \sum_{i=0}^{\infty} a_i(t) w_i(x), \quad (4)$$

or equivalently in vector notation,

$$w(x, t) = \underline{a}(t) \cdot \underline{w}(x). \quad (5)$$

Here  $u_c$  is the function representing the axial displacement associated with beam buckling,  $\underline{a}(t)$  is a vector which contains the mode amplitudes, and  $\underline{w}(x)$  is a vector of shape functions, which are the transverse displacements of the mode shapes. The buckled equilibrium transverse displacements are assumed to represent a fundamental mode of the dynamic

response of the system, with its contribution to the total displacements varying according to  $a_0(t)$ , and the subscript 0 has been assigned to it. Increasing indices in the summation (4) indicate increasing natural frequency for the associated mode shape. The shape of the first three mode shapes with the respective buckled equilibrium shape and axial load are shown in figure 6.

### 3.2. Kinetic energy

The kinetic energy can be expressed by superimposing the transverse beam motions onto the base excitation,  $y(t)$ :

$$\begin{aligned} T &:= \int_0^L \frac{1}{2} m(x) \left( \frac{\partial w}{\partial t} + \frac{\partial y}{\partial t} \right)^2 dx \\ &\approx \frac{m_b}{2} \int_0^{L_b} (\dot{w} + \dot{y})^2 dx + \frac{m_s}{2} \int_{L_s}^L (\dot{w} + \dot{y})^2 dx, \end{aligned} \quad (6)$$

where  $m_b$  and  $m_s$  are the mass per unit length of the bimorph and single layer, respectively. The time derivative of the displacement can be written as

$$\dot{w} = \dot{a}_0 w_0 + \sum_{i=1}^{\infty} \dot{a}_i w_i. \quad (7)$$

The buckled equilibrium displacement has been separated from the linear modes to preserve the orthogonality properties. We obtain

$$\begin{aligned} \dot{w}^2 &= \dot{a}_0^2 w_0^2 + 2 \sum_{i=1}^{\infty} (\dot{a}_i \dot{a}_0 w_i w_0) \\ &\quad + \sum_{i=1}^{\infty} \sum_{j=1}^{\infty} (\dot{a}_i \dot{a}_j w_i w_j). \end{aligned} \quad (8)$$

From the orthogonality condition (2), the last term integrates to zero when  $i \neq j$ . This allows the kinetic

energy to be calculated as

$$\begin{aligned}
T \approx & \frac{m_b}{2} \int_0^{L_b} \left[ a_0^2 w_0^2 + \sum_{i=1}^n (2\hat{a}_i a_0 w_i w_0 + \hat{a}_i^2 w_i^2) \right. \\
& \left. + \sum_{i=0}^n (2\hat{a}_i w_i \dot{y} + \dot{y}^2) \right] dx \\
& + \frac{m_s}{2} \int_{L_s}^L \left[ a_0^2 w_0^2 + \sum_{i=1}^n (2\hat{a}_i a_0 w_i w_0 + \hat{a}_i^2 w_i^2) \right. \\
& \left. + \sum_{i=0}^n (2\hat{a}_i w_i \dot{y} + \dot{y}^2) \right] dx, \quad (9)
\end{aligned}$$

where  $n$  is the number of mode shapes that we have included in a truncated calculation.

### 3.3. Potential energy

The potential energy has contributions from both mechanical and electrical domains. In the mechanical domain, the strain energy is calculated as one half the volume integral of the product of stress and strain. In the electrical domain, the energy is calculated as the negative of one half the volume ( $V$ ) integral of the product of electric displacement and electric field:

$$U = \frac{1}{2} \int_V \sigma \varepsilon \, dV - \frac{1}{2} \int_V DE \, dV, \quad (10)$$

where  $\sigma$  is the stress,  $\varepsilon$  is the strain,  $D$  is the electric displacement, and  $E$  is the electric field. Piezoelectric constitutive equations [8] describe elastic and dielectric behavior and provide the connection between the mechanical and electrical portions:

$$\sigma_{ij} = c_{ijkl}^E \varepsilon_{kl} - e_{kij} E_k, \quad (11)$$

$$D_i = e_{ikl} \varepsilon_{kl} + \epsilon_{ik}^E E_k, \quad (12)$$

where  $c_{ijkl}^E$  is the tensor of elastic constants evaluated at fixed electric field,  $e_{kij}$  is the tensor of piezoelectric coupling constants when electric field and strain are taken as the independent variables, and  $\epsilon_{ik}^E$  is the tensor of electric permittivity constants evaluated at fixed strain. Euler–Bernoulli beam theory assumes that all stress components are negligible except those in the axial direction. Piezoelectric theory defines the poling direction as the three-direction, which coincides in our case with the axial direction in a  $d_{33}$  beam configuration. The constitutive equations can therefore be reduced to

$$\begin{bmatrix} \sigma_3 \\ D_3 \end{bmatrix} = \begin{bmatrix} c_{33}^E & -e_{33} \\ e_{33} & \epsilon_{33}^E \end{bmatrix} \begin{bmatrix} \varepsilon_3 \\ E_3 \end{bmatrix}. \quad (13)$$

Piezoelectric constants are provided in a slightly different form, as seen in table 2. The necessary coefficients are calculated as [8]

$$c_{33}^E = Y, \quad (14)$$

$$e_{33} = d_{33} \cdot Y, \quad (15)$$

$$\epsilon_{33}^E = \epsilon_{33}^\sigma - d_{33}^2 \cdot Y, \quad (16)$$

**Table 2.** Piezoelectric constants provided by Advanced Ceramics Inc. [14].

Constant	Value	Units
$d_{33}$	375	pm V <sup>-1</sup>
$\epsilon_{33}^\sigma/\epsilon_0$	1725	n/a

where  $Y$  is the experimentally determined elastic modulus of the section being analyzed as presented in table 1 and  $\epsilon_{33}^\sigma$  is the dielectric permittivity in the poled direction at fixed stress. Combining (10) and (13), and dropping the subscripts we find that

$$\begin{aligned}
U = & \frac{1}{2} \int_V Y \varepsilon^2 \, dV - \int_V e \varepsilon E \, dV \\
& - \frac{1}{2} \int_V \epsilon E^2 \, dV. \quad (17)
\end{aligned}$$

First we will deal with the strain energy, then later we will come back to the electrical contributions to the potential energy.

**3.3.1. Equilibrium strain energy.** At equilibrium, the electric field and electric displacement are zero, and only the buckled mode shape contributes to the potential energy. Thus this potential energy can be expressed as

$$U_{eq} = \frac{1}{2} \int_V Y \varepsilon^2 \, dV. \quad (18)$$

Here the goal is to develop an expression for the strain energy that has the buckled equilibrium mode amplitude as the independent variable. In order for a double well potential to exist, the energy function must be at least quartic. Forcing the symmetric, stable equilibrium positions to occur at  $a_0 = \pm 1$ , the potential energy can be approximated as

$$\begin{aligned}
U_{eq} = & \frac{1}{2} \int_V Y \varepsilon^2 \, dV \approx \eta_0 \\
& - 2\beta a_0^2 + \beta a_0^4 + \mathcal{O}(a_0^6), \quad (19)
\end{aligned}$$

where  $\frac{\partial U_{eq}}{\partial a_0}$  must be equal to zero when evaluated at  $a_0 = \pm 1$ . From the FEA, there is a reference for the strain energy at two configurations: the buckled equilibrium position ( $a_0 = \pm 1$ ), and the constrained flat equilibrium ( $a_0 = 0$ ). Using these reference values allows one to solve for  $\beta$ .

**3.3.2. Dynamic contributions to strain energy.** We note that for strains to be infinitesimal we must have

$$\left| 2 \frac{\partial u}{\partial x} + \left( \frac{\partial u}{\partial x} \right)^2 + \left( \frac{\partial w}{\partial x} \right)^2 \right| \ll 1. \quad (20)$$

This can occur when

$$\left( \frac{\partial w}{\partial x} \right)^2 = \mathcal{O} \left( \frac{\partial u}{\partial x} \right) \ll 1. \quad (21)$$

These conditions preclude even moderately large transverse deflections when compared to the length of the beam. The

other possibility for fulfilling the infinitesimal strain condition is that

$$\frac{\partial u}{\partial x} < 0 \quad (22)$$

and the combination

$$2 \frac{\partial u}{\partial x} + \left( \frac{\partial u}{\partial x} \right)^2 + \left( \frac{\partial w}{\partial x} \right)^2 \quad (23)$$

is small because of cancellation of positive and negative terms. This can happen in buckled beams, but if this condition prevails and the beam oscillates from a positive deflection to a negative deflection by passing through its straight configuration, the axial strain could be large due to the absence of the positive transverse deflection term. However, if we assume that the oscillation from positive deflection to negative deflection occurs by a combination of modes of deformation, the beam may never be straight in such motion, and large deflections may then be permitted. This relieves us of the requirement (21), and instead we may rely on (20). Thus under assumptions of small strain and moderate rotation, we approximate the axial strain at any point from the Green-Lagrange strain tensor [16] as

$$\begin{aligned} \varepsilon \approx & \frac{\partial u_c}{\partial x} - z \frac{\partial^2 w}{\partial x^2} \\ & + \frac{1}{2} \left( \frac{\partial u_c}{\partial x} - z \frac{\partial^2 w}{\partial x^2} \right)^2 + \frac{1}{2} \left( \frac{\partial w}{\partial x} \right)^2, \end{aligned} \quad (24)$$

where  $z$  is the distance of the specified point from the neutral axis of the beam. FEA does not provide enough reference points to generate a full description of the strain energy using the amplitudes of the mode shapes. To overcome this obstacle, it is necessary to use analytic predictions to determine the shape of the energy surfaces. To generate these approximate surfaces, the buckled equilibrium amplitude will be fixed at unity, and two mode amplitudes varied while all other amplitudes are equal to zero. The resulting shape is then integrated over the approximate beam dimensions as

$$\Omega \approx \frac{1}{2} \int_V Y \varepsilon^2 dV, \quad (25)$$

where  $\varepsilon$  is as in (24). This produces an analytic prediction of the strain energy ( $\Omega$ ) at one particular combination of mode shapes. We repeat this procedure on a grid to span the maximum mode amplitudes observed in simulation, which is an iterative process. Now a surface has been produced describing the energy variation with two mode shapes about the buckled equilibrium. This surface is fit with a fourth-order polynomial in two variables, remembering that symmetric solutions dictate which terms are needed. As an example, the polynomial describing the variation of strain energy with

variation of modes  $i$  and  $j$  is of the form:

$$\begin{aligned} \Omega(a_i, a_j, a_0) \approx & \eta_1 + m_1 a_i^2 + m_2 a_j^2 + m_3 a_i a_j \\ & + m_4 a_0 a_i^2 a_j + m_5 a_0 a_i a_j^2 \\ & + m_6 a_0 a_i^3 + m_7 a_0 a_j^3 + m_8 a_i^2 a_j^2 \\ & + m_9 a_i^3 a_j + m_{10} a_i a_j^3 + m_{11} a_i^4 + m_{12} a_j^4, \end{aligned} \quad (26)$$

where the  $m$ 's are the coefficients to be solved for in the fit. Repeating this procedure for all combinations of mode shapes, all of the planes can be combined to produce a polynomial fit of the strain energy surface as a function of the mode amplitudes. The approximate nature of this calculation leaves a discrepancy between the strain energy at equilibrium as calculated above and the FEA result. To ensure consistency, the strain energy surface is multiplied by an order one constant to make the strain energy at equilibrium equal to the FEA results.

**3.3.3. Piezoelectric terms.** Terms containing piezoelectric coupling and capacitive energy storage are:

$$U_{\text{piezo}} = -\frac{1}{2} \int_V \varepsilon E^2 dV - \int_V e \varepsilon E dV. \quad (27)$$

The first term captures the electrical energy stored in the capacitance of the piezoelectric material, which can be expanded as

$$\begin{aligned} \frac{1}{2} \int_V \varepsilon E^2 dV \approx & \frac{\varepsilon E_B^2}{2} \left[ \int_{P_1} dV + \int_{P_2} dV \right] \\ & + \frac{\varepsilon E_S^2}{2} \int_{P_3} dV, \end{aligned} \quad (28)$$

where  $P_1$  and  $P_2$  are the two piezoelectric layers of the bimorph, and  $P_3$  is the single layer section of the beam. Separate electrical circuits are defined on the bimorph section and the single-layer section, therefore the electric field variable has been divided into two contributions, one from each beam section. Calculation of capacitive energy storage is easily accomplished utilizing the volume of each piezoelectric beam. The coupling between the mechanical and electrical domains is contained in the second term and can be expanded as

$$\begin{aligned} \int_V e \varepsilon E dV \approx & E_B \left( e_1 \int_{P_1} \varepsilon dV + e_2 \int_{P_2} \varepsilon dV \right) \\ & + e_3 E_S \int_{P_3} \varepsilon dV. \end{aligned} \quad (29)$$

Note that the piezoelectric coupling coefficient  $e$  has been separated into different values for each section of the beam. The absolute value of this parameter is the same for all three layers, but due to coupling directions and orientation, the sign of the coefficient can change. In the single-layer section, we will define  $e_3$  as the same as the coupling constant  $e$ . In the bimorph section, the coupling in the two layers is reversed, so

we will define  $e_1 = e$  and  $e_2 = -e$ . This produces

$$\int_V e \varepsilon E \, dV \approx e \left[ E_B \left( \int_{P_1} \varepsilon \, dV - \int_{P_2} \varepsilon \, dV \right) + E_S \int_{P_3} \varepsilon \, dV \right]. \quad (30)$$

The contribution from the single layer is the electric field times the membrane stretch. This integral will be converted to a quadratic polynomial of the mode amplitudes by generating linear combinations of the mode shapes, which is accomplished by calculating the arc length ( $s$ ) of the resulting shape, dividing by the natural length to calculate the stretch ratio, then taking the natural logarithm of the stretch ratio to determine the volume average axial strain:

$$s(a_0, a_1, \dots, a_n) = \int_{L_S}^L \sqrt{1 + \left( \frac{\partial u}{\partial x} \right)^2} \, dx, \quad (31)$$

$$\frac{1}{V} \int_{P_3} \varepsilon \, dV = \ln \left( \frac{s(a_0, a_1, \dots, a_n)}{L_0} \right), \quad (32)$$

where  $L_0$  is the natural, unstretched length of the beam. Repeating the above process to span the expected mode amplitudes generates a surface which is fit with a quadratic polynomial with the mode amplitudes as the independent variables:

$$\int_{P_3} \varepsilon \, dV \approx c_1 + [c_3]: [\underline{a}^T \underline{a}], \quad (33)$$

where ‘:’ indicates a matrix dot product, or Frobenius inner product. The  $d_{33}$  beam is configured such that a voltage difference is detected at the electrodes in response to an axial deformation; in the bimorph beam this causes a voltage to develop at the electrodes in response to a bending deformation, and we realize cancellation of any contribution from an axial load. Therefore to leading order the mode amplitudes will affect this integral in a linear fashion:

$$\int_{P_1} \varepsilon \, dV - \int_{P_2} \varepsilon \, dV \approx \underline{a} \cdot \underline{c}_2, \quad (34)$$

where  $\underline{c}_2$  is a vector of coefficients. The integrals on the left-hand side of this equation can be evaluated at various combinations of amplitudes, and this provides solutions for these coefficients. The total potential energy can now be expressed as

$$U \approx -2\beta a_0^2 + \beta a_0^4 + \Omega - \frac{\varepsilon E_B^2}{2} [V_{P_1} + V_{P_2}] + \frac{\varepsilon E_S^2}{2} V_{P_3} - e [E_B (\underline{a} \cdot \underline{c}_2) + E_S (c_1 + [c_3]: [\underline{a}^T \underline{a}])]. \quad (35)$$

### 3.4. Equations of motion

With the kinetic energy as defined in (9), and the potential energy defined as (35), a Lagrangian function will be used to derive equations of motion based on the mode amplitudes.

The Lagrangian  $\mathcal{L}$  is computed as the kinetic energy minus the potential energy, and the equations of motion are generated via the Euler–Lagrange equation as follows:

$$\frac{d}{dt} \left( \frac{\partial \mathcal{L}}{\partial \dot{a}_i} \right) - \frac{\partial \mathcal{L}}{\partial a_i} = \zeta_i \dot{a}_i(t), \quad i = 0, \dots, n, \quad (36)$$

$$\frac{d}{dt} \left( \frac{\partial \mathcal{L}}{\partial \dot{F}_j} \right) - \frac{\partial \mathcal{L}}{\partial F_j} = \frac{\dot{F}_j}{R_j}, \quad j = B, S, \quad (37)$$

where  $F$  is the time integral of the voltage,  $v$ , called the flux linkage ( $v_j = \dot{F}_j$ ). The terms on the right side of the equations represent losses in the system. Modes of the system are assumed to have damping losses proportional to their velocity,  $\zeta_i$  corresponding to the  $i$ th mode. Current flowing out of the system removes energy from the electrical portion. Deriving a model using a buckled equilibrium shape plus the first three mode shapes (referred to as a three-mode model), we produce equations of the form:

$$\begin{aligned} \ddot{a}_i = & b_{(i,1)} a_0 + b_{(i,2)} a_0^3 + b_{(i,3)} a_1 + b_{(i,4)} a_0 a_1^2 + b_{(i,5)} a_1^2 \\ & + b_{(i,6)} a_2 + b_{(i,7)} a_0 a_1 a_2 + b_{(i,8)} a_1^2 a_2 + b_{(i,9)} a_0 a_2^2 \\ & + b_{(i,10)} a_1 a_2^2 + b_{(i,11)} a_2^3 + b_{(i,12)} a_3 + b_{(i,13)} a_0 a_1 a_3 \\ & + b_{(i,14)} a_1^2 a_3 + b_{(i,15)} a_0 a_2 a_3 + b_{(i,16)} a_2^2 a_3 \\ & + b_{(i,17)} a_0 a_3^2 + b_{(i,18)} a_1 a_3^2 + b_{(i,19)} a_2 a_3^2 + b_{(i,20)} a_3^3 \\ & + b_{(i,21)} A \omega^2 \sin \omega t + b_{(i,22)} v_B + b_{(i,23)} a_0 v_S \\ & + b_{(i,24)} a_1 v_S + b_{(i,25)} a_2 v_S + b_{(i,26)} a_3 v_S \\ & + b_{(i,27)} \dot{a}_0 + b_{(i,28)} \dot{a}_1 + b_{(i,29)} \dot{a}_2 + b_{(i,30)} \dot{a}_3, \end{aligned} \quad (38)$$

$$v_B = d_0 \dot{a}_0 + d_1 \dot{a}_1 + d_2 \dot{a}_2 + d_3 \dot{a}_3 + d_4 v_B, \quad (39)$$

$$\begin{aligned} v_S = & \dot{a}_0 (h_0 a_0 + h_1 a_1 + h_2 a_2 + h_3 a_3) \\ & + \dot{a}_1 (h_4 a_0 + h_5 a_1 + h_6 a_2 + h_7 a_3) \\ & + \dot{a}_2 (h_8 a_0 + h_9 a_1 + h_{10} a_2 + h_{11} a_3) \\ & + \dot{a}_3 (h_{12} a_0 + h_{13} a_1 + h_{14} a_2 + h_{15} a_3) + h_{16} v_S, \end{aligned} \quad (40)$$

where  $b$  is a matrix of coefficients with as many rows as shape functions, and  $d$  and  $h$  are vectors of coefficients. This three-mode model consists of ten degrees of freedom: eight for the shape functions and two for the piezoelectric voltages. The primary motivation for generation of this model is to replicate the behavior that generates the transition to high power output to allow further dynamic analysis and optimization of the system. Therefore, the modes are selected by determining the minimum number required to replicate experimental behavior while keeping the degrees of freedom within the range which can be dynamically analyzed.

## 4. Comparison with experimental results

Evaluation of the model requires determination of damping coefficients. Experimental results only provide voltage outputs, and therefore provide insufficient data for determination of modes or their respective damping ratios. Damping coefficients have been adjusted to match the input power level at

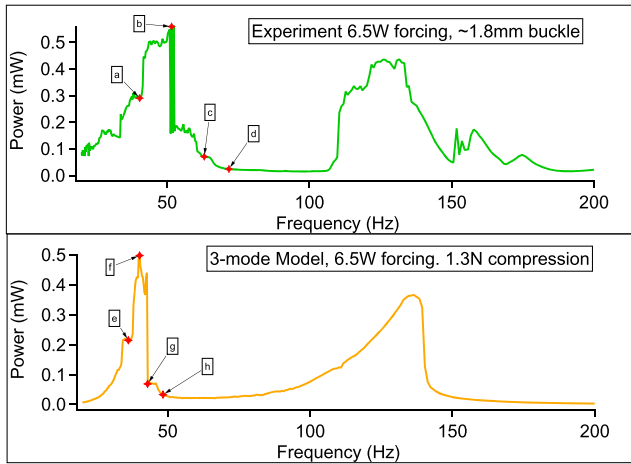


**Figure 7.** A comparison of the power output of the experiment and the predicted output of the model. Points marked as (a) through (h) will be used to compare dynamic behavior of the experimental system and the model, as shown in figure 8.

which inter-well oscillations begin, while ensuring that higher mode numbers are increasingly damped and the unforced system when perturbed returns to equilibrium quickly. The resulting coefficients can be seen in table 3. Evaluation of the Jacobian matrix at one of the stable equilibrium positions shows that this system is stiff, with the eigenvalues presented in table 4. To deal with this, a backwards differentiation formula is used for numerical integration, with an analytic Jacobian to aid in convergence.

Traditionally frequency response measurements present data as a ratio between the input and the output amplitude, commonly presented as decibels. Linear systems that have the property of superposition can be accurately described with this method, but nonlinear systems do not possess the property of superposition, so presenting data in this way can be misleading. Additionally, nonlinear systems often produce non-sinusoidal signals where amplitude is poorly defined. A more appropriate method for comparing nonlinear systems is to ensure that the root mean square (rms) excitation power level is constant as the frequency is varied, requiring the forcing amplitude to vary as well as the frequency. This allows rms power outputs at different frequencies to be compared without skewing the results. In this paper all power figures are reported as rms values.

The comparison of power output of the model and experiment, both in response to 6.5 W of input power, can be seen in figure 7. The experimental setup is buckled to a transverse maximum displacement of approximately 1.8 mm with an error bound of approximately 0.5 mm, while the model is specified to have a compressive force of 1.3 N, which results in 1.34 mm maximum transverse deflection, which is within the error bound of the experiment. Perfect agreement of results is not expected due to the complex nature of the system and the severe truncation associated with our low-order model. Nevertheless every attempt has been made in the model to keep results for all parameters within the expected error bounds of the experiment.

**Table 3.** Damping ratios prescribed to provide inter-well behavior at similar excitation level to experimental observations.

Mode ( $i$ )	Damping ratio ( $\zeta_i$ )
0	$1 \times 10^{-11}$
1	$12 \times 10^{-8}$
2	$2 \times 10^7$
3	$2 \times 10^5$

**Table 4.** Eigenvalues of the Jacobian matrix at stable equilibrium.

Eigenvalues at equilibrium
-76015
-55787
-27893
-4.73
$-49.05 \pm 2185i$
$-75.67 \pm 719.3i$
$-16.84 \pm 130.5i$

Phase portraits for dynamic comparison are constructed by plotting the voltage measured across the single layer beam against the voltage measured across the bimorph. The system is first allowed to evolve for several seconds to allow any transient to die out, then when a consistent behavior is seen, data are gathered by measuring the voltage across a 2.2 k $\Omega$  resistor. The system is then strobed at the forcing frequency to create a Poincaré map, which is overlaid on the phase portrait. These plots are shown in figure 8, and it can be seen that similar behavior in the chaotic region occurs in the model and the experiment. The system starts as a twisted period-1 orbit which repeats indefinitely as seen in panels (a) and (e) of figure 8. As the forcing frequency is increased there is a torus which loses any recognizable structure and ceases to repeat itself, resulting in chaotic behavior as seen in panels (b) and (f). Further increase of the forcing frequency returns to a twisted periodic orbit (panels (c) and (g)), which simplifies and untwists until a much simpler period-1 orbit is achieved which persists throughout the low power region, as seen in panels (d) and (h). Note that the experimental system contains much more high frequency content than the model; however the model successfully captures the essential behavior of the system.

The power output of the model is indicated as being slightly lower than is measured in the experiment, which is most likely due to the use of the nominal piezoelectric coupling coefficient, which is expected to have some variation. Note that the high power output frequencies for the model and experiment are slightly different, but indicate the same sort of behavior around the high power output areas. The lower frequency peak exhibits shoulders around the highest output area in both model and experiment, but the model does not have quite as much bandwidth as the experimental peak. This is presumably due to the severe truncation in the model used to reduce the system from infinite dimensional to ten degrees of freedom. The second peak around 120–140 Hz also demonstrates wider bandwidth for the experiment than the model, and

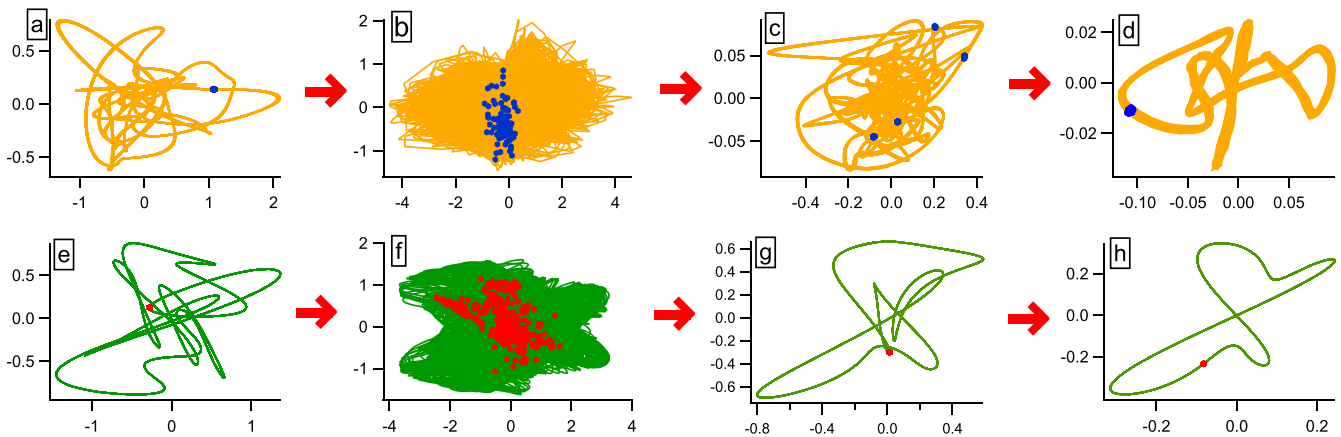


**Figure 8.** Phase plots around a chaotic regime in the experiment and the model. Phase plots are generated with voltage output from the single layer beam on the horizontal axis and voltage from the bimorph on the vertical axis. Poincaré maps are overlaid on phase space plots, and the letter in each panel corresponds to the marked locations in figure 7. Upper plots represent the experiment, lower plots represent the model. At frequencies lower than the chaotic regime, both have a complex period-1 orbit. Increasing the forcing frequency causes chaotic behavior, producing phase plots and Poincaré maps that appear to have no structure. Continued increase of the forcing frequency returns the behavior to a periodic response, which simplifies as the forcing frequency moves further above chaos until a relatively simple period-1 orbit is achieved.

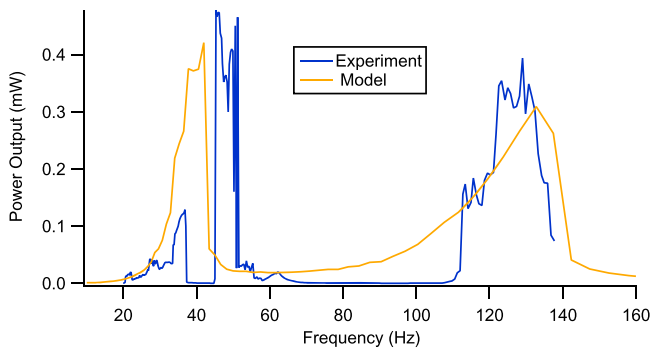


**Figure 9.** A comparison of the power output of the experiment and the predicted output of the model in response to 5.5 W of rms input power.

any higher frequency peaks are very attenuated in the model. As the driving frequency of the system increases, the number of modes required to capture the behavior seen in the experiment goes up. However, our model has been truncated to allow accurate analysis of the lowest lobe of power output. In spite of these discrepancies, the model appears to capture the critical behavior of the system and gives a good indication of the power output over a significant frequency range.

A second demonstration of the ability of the model to provide conservative estimates of both power output and bandwidth can be seen in figure 9. This response is based on the same beam configuration, but at a lower driving power of 5.5 W. As the input power level is lowered further, the beam settles into single-well behavior around 55 Hz and power output drops off significantly.

## 5. Conclusion

A model has been generated for a complex, nonlinear energy harvesting system. FEA was used to determine a basis for

projecting the system dynamics onto, as well as a reference for stresses and strains in the equilibrium positions. This approach allows a system to be modeled when analytic solutions are unavailable. It was found that to properly capture the small strain snap-through effects of the system, it is necessary to keep several modes in addition to the buckled equilibrium shape so that the system never passes through the flat, unstable equilibrium where the strains would be relatively high. The model demonstrates good quantitative agreement with the power output of the experiment in both power level and frequency of occurrence. Experimental transitions between dynamic behavior patterns are replicated closely, indicating that the model is appropriate for dynamic analysis of the underlying phenomena. Further work on this model will be focused on a detailed dynamic analysis with a goal of determining how design parameters can be tuned to optimize energy harvesting performance. We note that nominal material parameters are used in this paper; it was not necessary to tune these for better agreement. Overall, the model provides a source for understanding and optimizing energy harvesting ability with a system that exhibits a much broader response than a linear resonator.

## Acknowledgments

This work was supported by the National Science Foundation under grant NSF-1131052.

## References

- [1] Roundy S, Wright P K and Rabaey J 2003 A study of low level vibrations as a power source for wireless sensor nodes *Comput. Commun.* **26** 1131–44

- [2] Zhu Y, Zu J and Su W 2013 Broadband energy harvesting through a piezoelectric beam subjected to dynamic compressive loading *Smart Mater. Struct.* **22** 045007
- [3] Kim S B, Park J, Kim S H, Ahn H, Wickle H C and Kim D J 2012 Modeling and evaluation of  $d_{33}$  mode piezoelectric energy harvesters *J. Micromech. Microeng.* **22** 105013
- [4] Arrieta A F, Delpero T, Bergamini A E and Ermanni P 2013 Broadband vibration energy harvesting based on cantilevered piezoelectric bi-stable composites *Appl. Phys. Lett.* **102** 173904
- [5] Hu Y and Xu Y 2014 A wideband vibration energy harvester based on a folded asymmetric gapped cantilever *Appl. Phys. Lett.* **104** 053902
- [6] Xu C, Liang Z, Ren B, Di W, Luo H, Wang D, Wang K and Chen Z 2013 Bi-stable energy harvesting based on a simply supported piezoelectric buckled beam *J. Appl. Phys.* **114** 114507
- [7] Gao X, Shih W H and Shih W Y 2010 Vibration energy harvesting using piezoelectric unimorph cantilevers with unequal piezoelectric and nonpiezoelectric lengths *Appl. Phys. Lett.* **97** 233503
- [8] Erturk A and Inman D J 2011 *Piezoelectric Energy Harvesting* (Chichester: Wiley)
- [9] Harne R L and Wang K W 2013 A review of the recent research on vibration energy harvesting via bistable systems *Smart Mater. Struct.* **22** 023001
- [10] Nayfeh A H, Kreider W and Anderson T J 1995 Investigation of natural frequencies and mode shapes of buckled beams *AIAA J.* **6** 33
- [11] Masana R and Daqaq M F 2010 Electromechanical modeling and nonlinear analysis of axially loaded energy harvesters *J. Vib. Acoust.* **133** 011007
- [12] Sneller A J, Cetta P and Mann B P 2011 Experimental investigation of a post-buckled piezoelectric beam with an attached central mass used to harvest energy *Proc. IMechE I: J. Syst. Control Eng.* **225** 497
- [13] Cottone F, Gammaitoni L, Vocca H and Ferrari M 2012 Piezoelectric buckled beams for random vibration energy harvesting *Smart Mater. Struct.* **21** 035021
- [14] [www.advancedceramics.com](http://www.advancedceramics.com)
- [15] Van Blarigan L, Danzl P and Moehlis J 2012 A broadband vibrational energy harvester *Appl. Phys. Lett.* **100** 253904
- [16] Szilard R 1974 *Theory and Analysis of Plates: Classical and Numerical Methods* (Englewood Cliffs, NJ: Prentice-Hall)
- [17] ABAQUS Documentation 2014 *Dassault Systems* (Providence, RI)